

<https://doi.org/10.1038/s42005-024-01845-w>

Simulating unsteady flows on a superconducting quantum processor

Check for updates

Zhaoyuan Meng^{1,5}, Jiarun Zhong^{2,5}, Shibo Xu^{2,5}, Ke Wang², Jiachen Chen², Feitong Jin², Xuhao Zhu², Yu Gao², Yaozu Wu², Chuanyu Zhang², Ning Wang², Yiren Zou², Aosai Zhang², Zhengyi Cui², Fanhao Shen², Zehang Bao², Zitian Zhu², Ziqi Tan², Tingting Li², Pengfei Zhang², Shiyong Xiong³, Hekang Li², Qiujiang Guo², Zhen Wang², Chao Song²✉, H. Wang² & Yue Yang^{1,4}✉

Recent advancements of quantum technologies have triggered tremendous interest in exploring practical quantum advantage. The simulation of fluid dynamics, a highly challenging problem in classical physics but vital for practical applications, emerges as a potential direction. Here, we report an experiment on the digital simulation of unsteady flows with a superconducting quantum processor. The quantum algorithm is based on the Hamiltonian simulation using the hydrodynamic formulation of the Schrödinger equation. With the median fidelities of 99.97% and 99.67% for parallel single- and two-qubit gates respectively, we simulate the dynamics of a two-dimensional (2D) compressible diverging flow and a 2D decaying vortex with ten qubits. Note that the former case is an inviscid potential flow, and the latter one is an artificial vortical flow with an external body force. The experimental results well capture the temporal evolution of averaged density and momentum profiles, and qualitatively reproduce spatial flow fields with moderate noises. This work demonstrates the potential of quantum computing in simulating more complex flows, such as turbulence, for practical applications.

Simulating fluid dynamics on classical computers at a high Reynolds number (Re) has significant applications in various fields, such as weather forecasting and airplane design. However, it remains challenging due to the wide range of spatial and temporal scales involved in turbulent flows. Its computational cost, scaling with $\mathcal{O}(Re^3)$ operations for the direct numerical simulation of turbulence¹, is prohibitively expensive for engineering applications^{2,3}. The emergence of quantum computing has garnered attention as a potential solution to the computational limitations in classical computing^{4–7}. Leveraging laws of quantum mechanics such as superposition and entanglement, a quantum processor can manipulate exponentially large degrees of freedom that are intractable on classical computers, making it a promising platform for empowering the next-generation simulation method for fluid dynamics^{8–10}. In particular, quantum computing of turbulence, one of the most challenging problems in classical physics¹¹, can serve as a compelling demonstration of quantum utility and practical quantum advantage^{12–15}.

There have been two major approaches to the quantum simulation of fluid dynamics. Based on solving the governing equations for fluids, hybrid quantum-classical algorithms are proposed^{10,16–27}, where quantum

computing is employed to handle highly parallelizable operations (e.g., solving linear systems^{28,29}). The efficiencies of these methods are often burdened by the frequent data exchanges between classical and quantum hardware, as the preparation and statistical measurement of arbitrary quantum state can be more time-consuming than the calculation procedure^{9,30}. Moreover, for the present noisy intermediate-scale quantum (NISQ) devices, the state preparation and measurement (SPAM) errors could accumulate during the time-marching in these algorithms, limiting their accuracy for near-term applications^{31,32}. To alleviate these problems, Hamiltonian simulation, which has been widely used in exploring quantum many-body physics on NISQ devices^{13,32–36}, was proposed as a promising approach to simulate fluid dynamics^{37–52}. In this simulation, a fluid flow is mapped to a quantum system, which can then be evolved and detected on a quantum processor without invoking intermediate quantum state measurement and re-initialization.

However, obstacles remain. First, general fluid dynamics has non-linear characteristics, while quantum operations except measurement are linear. Incorporating the nonlinearity into a quantum algorithm poses significant challenges. Second, while minimizing the influence of

¹State Key Laboratory for Turbulence and Complex Systems, College of Engineering, Peking University, Beijing, 100871, China. ²School of Physics, ZJU-Hangzhou Global Scientific and Technological Innovation Center, and Zhejiang Key Laboratory of Micro-nano Quantum Chips and Quantum Control, Zhejiang University, Hangzhou, 310027, China. ³Department of Engineering Mechanics, School of Aeronautics and Astronautics, Zhejiang University, Hangzhou, 310027, China. ⁴HEDPS-CAPT, Peking University, Beijing, 100871, China. ⁵These authors contributed equally: Zhaoyuan Meng, Jiarun Zhong, Shibo Xu.

✉ e-mail: chaosong@zju.edu.cn; yyg@pku.edu.cn

SPAM errors, the Hamiltonian simulation can still be affected by the inevitable errors occurred during the execution of quantum evolution on the NISQ devices. A proof-of-principle demonstration of the capability of the contemporary NISQ devices in simulating fluid dynamics remains elusive. Here we report the end-to-end quantum simulation of two-dimensional (2D) unsteady flows, discretized spatially with up to 1024 grid points, on a superconducting quantum processor. We first consider a simple compressible diverging flow and reveal its dynamics according to the hydrodynamic formulation of the corresponding Schrödinger equation. Then, by involving the two-component wave function, we realize the quantum simulation of a decaying vortex with nonlinear vortex dynamics.

As sketched in Fig. 1, the simulation (referred to as “experiment” below) is implemented with ten qubits on a superconducting processor^{53–55}. Through optimizing device fabrication and carefully tuning controlling parameters, we realize median fidelities of 99.97% (99.67%) and 99.3% for parallel single- (two-) qubit gates and measurements, respectively. With the high fidelities and by employing efficient quantum circuits for state preparation and Hamiltonian simulation, we obtain the average density and momentum profiles that well capture key features of the targeting flows. The present study demonstrates the capability of NISQ devices to simulate practical fluid flows, indicating the potential of quantum computing in exploring turbulent flows.

Results

Framework and experimental setup

In our algorithm, we encode the flow state into the n_ψ -component wave function $\psi \equiv [\psi_1, \dots, \psi_{n_\psi}]^T$, with $n_\psi \in \{1, 2\}$. Based on the generalized Madelung transform, the flow density and momentum can be extracted as

$\rho \equiv \sum_{j=1}^{n_\psi} |\psi_j|^2$ and $J \equiv \frac{i\hbar}{2m} \sum_{j=1}^{n_\psi} (\psi_j \nabla \psi_j^* - \psi_j^* \nabla \psi_j)$, respectively^{37,45,47}. Without loss of generality, we set the reduced Planck constant $\hbar = 1$ and the particle mass $m = 1$. The fluid velocity and vorticity are defined by $\mathbf{u} \equiv J/\rho$ and $\boldsymbol{\omega} \equiv \nabla \times \mathbf{u}$, respectively. Note that for a single-component wave function ψ , the velocity can be expressed as $\mathbf{u} = \frac{i}{2} \nabla \log \frac{\psi^*}{\psi}$, leading to $\boldsymbol{\omega} = \mathbf{0}$. To introduce finite vorticity, we need $n_\psi = 2^{45}$. We simulate fluid dynamics by evolving the wave function under the Hamiltonian $H = -\nabla^2/2 + V$, where the potential V , which may contain interaction terms among different wave-function components, gives the body force in the fluid flow⁴⁵. Using the Trotter decomposition⁵⁶, the evolution of the wave function can be approximated by a series of unitary operators (see Supplementary Note 1 for details).

In this work, we focus on the dynamics of 2D flows without conservative body forces in a periodic box $\mathbf{x} \in [-\pi, \pi]^2$, which is discretized into $2^{n_x} \times 2^{n_y}$ uniform grid points. The corresponding wave function of each component can be expressed in the computational basis of $n_x + n_y$ qubits as

$$|\psi_j(t)\rangle = \frac{1}{\|\psi_j\|_2} \sum_{l=0}^{2^{n_y}-1} \sum_{k=0}^{2^{n_x}-1} \psi_j(x_k, y_l, t) |k + 2^{n_x}l\rangle, \quad (1)$$

where the coordinates $x_k = -\pi + k\Delta x$ and $y_l = -\pi + l\Delta y$, with $\Delta x = 2\pi/2^{n_x}$ and $\Delta y = 2\pi/2^{n_y}$, respectively. For vortical flows, an additional qubit is required to encode the two-component wave function. In the absence of conservative body forces, the Hamiltonian reduces to $H = -(\partial_x^2 + \partial_y^2)/2$. The corresponding evolution can be realized without Trotterization as

$$e^{-iHt} = e^{i\partial_x^2 t/2} e^{i\partial_y^2 t/2} = U_x(t)U_y(t). \quad (2)$$

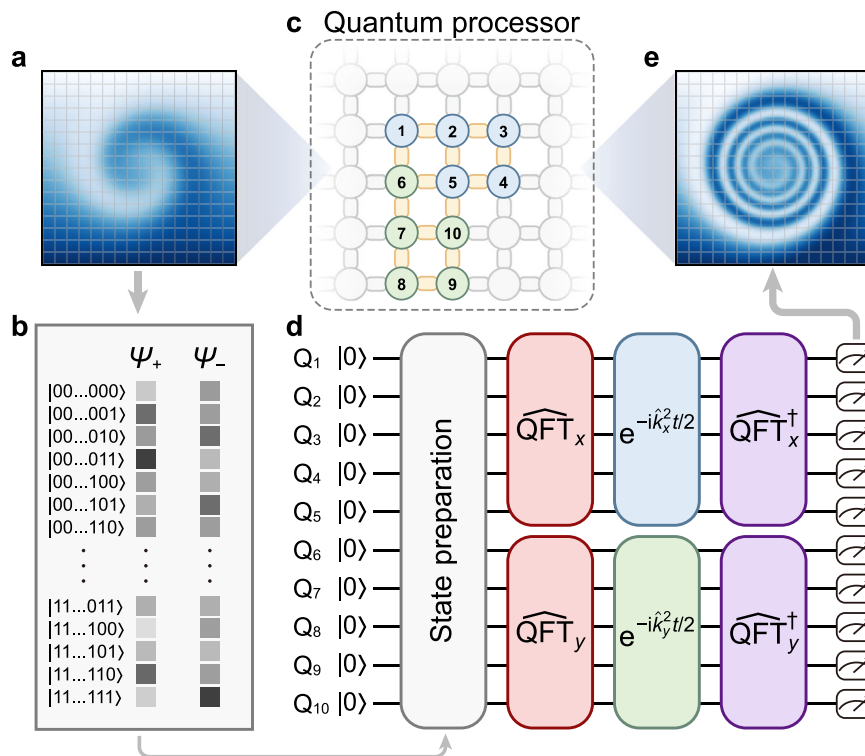


Fig. 1 | Schematic for the quantum simulation of fluid dynamics. The initial flow field (exemplified pictorially by a spiral vortex) discretized on a uniform grid in (a) is encoded by the multi-component wave function in (b), followed by state preparation. c Sketch of device topology. Qubits (circles) are arranged in a square lattice and connected through tunable couplers (bars). The ten qubits used here are labeled by Q₁–Q₅ (blue) and Q₆–Q₁₀ (green), encoding the wave function in the x - and y -directions, respectively. d Sketch of the quantum circuit for simulating the 2D

unsteady flows. The Hamiltonian simulation is realized by transforming a flow state into the momentum space with quantum Fourier transforms $\widehat{\text{QFT}}_x$ and $\widehat{\text{QFT}}_y$, applying unitary evolutions $e^{-ik_x^2 t/2}$ and $e^{-ik_y^2 t/2}$, and finally transforming the state back to the coordinate space. The circuit is further compiled with native gate sets (arbitrary single-qubit gates and two-qubit CZ gate) before the experimental execution. e At a given time t , the flow field is extracted by measuring a specific set of Pauli strings.

In the computational basis, the evolution operators can be digitized according to

$$U_\alpha(t) = \widehat{\text{QFT}}_\alpha^\dagger e^{-ik_\alpha t/2} \widehat{\text{QFT}}_\alpha, \quad (3)$$

where $\widehat{\text{QFT}}_\alpha$ denotes the unitary of quantum Fourier transform along the direction $\alpha \in \{x, y\}$, and the wavenumber is given by

$$\hat{k}_\alpha = -\frac{1}{2} \left(I_{2^{n_\alpha}} + \sum_{j=1}^{n_\alpha} 2^{n_\alpha-j} \hat{Z}_j \right) + 2^{n_\alpha} \hat{Z}_1. \quad (4)$$

Here, \hat{Z}_j denotes the Pauli operator of the j -th qubit and $I_{2^{n_\alpha}}$ the $2^{n_\alpha} \times 2^{n_\alpha}$ identity matrix. See Supplementary Note 2 for detailed derivations. The overall quantum circuit for simulating 2D unsteady flows is shown in Fig. 1d.

We implement the algorithm on a flip-chip superconducting quantum processor⁵³ using ten frequency-tunable transmon qubits labeled as Q_j for $j = 1-10$, as sketched in Fig. 1c. In the simulation, we set $n_x = n_y = 5$, corresponding to a solution domain with $2^5 \times 2^5 = 32^2$ grid points. Each qubit is individually controlled and readout. The nearest-neighboring qubits are capacitively connected through a tunable coupler, which is also a transmon qubit, for turning on and off the effective coupling between the two qubits. The single-qubit gate is realized by applying a 30 ns-long Gaussian-shaped microwave pulse with DRAG correction⁵⁷. The two-qubit CZ gate, with a length of 40 ns, is realized by carefully tuning the frequencies and coupling strength of the neighboring qubits to enable a closed-cycle diabatic transition of $|11\rangle \leftrightarrow |20\rangle$ (or $|02\rangle$)⁵⁸. The median parallel single- and two-qubit

gate fidelities are 99.97% and 99.67%, respectively. See Supplementary Note 3 for details.

Simulation of a diverging flow

As a first example, we demonstrate the quantum simulation of a 2D unsteady diverging flow, which is a simple model of nozzle in compressible potential flow. The flow is initially uniform in the x -direction, with mass concentrated near $y = 0$, which is described by a density of $\rho(x, y, 0) = e^{-y^2}$ and a velocity of $\mathbf{u}(x, y, 0) = \mathbf{e}_x$. The flow has the vanishing vorticity and can be encoded into a single-component wave function $\psi(x, y, 0) = e^{-y^2+ix}$. In practice, we use CPFlow⁵⁹ to synthesize the quantum circuit for initial state preparation, which fits the native gate set (i.e., arbitrary single-qubit gates and two-qubit CZ gates) and qubit layout topology of our device with minimal numbers of CZ gates. With an optimal depth of 13, the resulting circuit can generate a quantum state with an overlap above 0.999 to the target one in the ideal case (i.e., without any gate errors). After preparing the initial state, we apply quantum circuits of the evolution unitaries with specific times of $t = 0, \pi/4$ and $\pi/2$, respectively. The evolution circuits are also optimized with CPFlow, leading to a total circuit depth of around 30. To verify the simulation, we fully characterize the flow by measuring both the density and momentum distributions. While the density can be directly measured in the Z basis, the detection of the momentum requires measuring the quantum state in 62 different bases (see Supplementary Note 3 for details).

Figure 2a–c show the experimental data for the evolution of the density contour with streamlines for the diverging flow. Under the symmetry with respect to $y = 0$, the experimental data (lower half) is compared with the ideal result (upper half) from the exact solution in Eq. (S17) in Supplementary

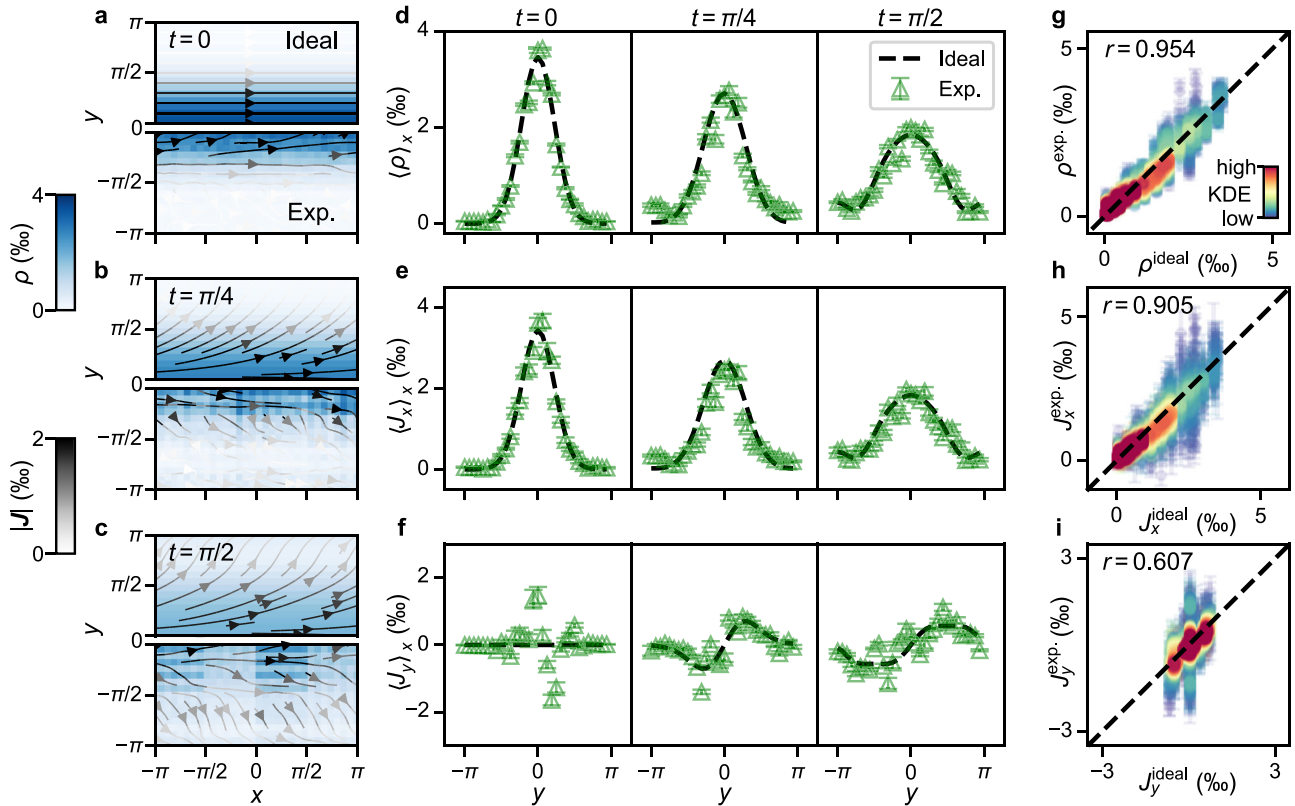


Fig. 2 | Comparison of experimental results on the superconducting quantum processor with the ideal ones for the 2D diverging flow. Density contours and streamlines are shown at (a) $t = 0$, (b) $t = \pi/4$, and (c) $t = \pi/2$. The flow is symmetric about $y = 0$ (upper panel: exact solution; lower panel: experimental measurement). The streamlines are color-coded by the momentum magnitude. **d–f** The x -averaged profiles for ρ , J_x , and J_y at $t = 0, \pi/4$, and $\pi/2$ (dashed lines: exact solution; triangles: experimental measurement with error bars denoting one standard deviation). The

density and momentum are obtained with 10^5 measurement shots, and the experiment is repeated for five times. **g–i** Scatter plots comparing ideal and experimental values for ρ , J_x , and J_y at $t = 0, \pi/4$, and $\pi/2$, along with the correlation coefficients (marked at the upper left). Data point density is color-coded by the kernel density estimation (KDE) from low (purple) to high (red) values.

Note 2. The mass diffusion accompanies the momentum diffusion from the central region near $y = 0$ to lateral sides. The experimental data exhibit qualitative agreements with ideal distributions. The discrepancies are mainly due to quantum gate errors, as even a single-qubit gate error of 5×10^{-4} can cause the stripe-like artifacts in experimental density contours (see Supplementary Note 4). Figure 2d–f plot profiles of ρ as well as two momentum components J_x and J_y . The profiles are averaged in the x -direction due to the homogeneity in x in this diverging flow. Their experimental and ideal results show good agreements. Thus, the quantum simulation on the NISQ device is able to predict unsteady flow evolution. Figure 2g–i present scatter plots comparing ideal and experimental values of ρ , J_x , and J_y at different times. A majority of data points, indicated by red for high data point density, align closely with the diagonal. In Fig. 2g, h, a considerable portion of experimental data falls below the actual values (orange), suggesting the effect of noises akin to filtering on the data. The correlation coefficients between the experimental and ideal values of ρ , J_x , and J_y are 0.954, 0.905, and 0.607, respectively. The notable error for J_y data is likely due to that the small value of J_y is prone to be influenced by noises (detailed in Supplementary Note 4).

Simulation of a decaying vortex

Next, we simulate a 2D vortex, a simple model of tornado and whirlpool, in the Schrödinger flow⁴⁵ (detailed in Supplementary Note 2). We construct the vortex via rational maps⁶⁰ in the periodic domain, which features a decaying vorticity profile $f(r) = e^{-(r/3)^2}$ along the radial distance $r = \sqrt{x^2 + y^2}$. Denoting the two components of the wave function as ψ_+ and ψ_- , the initial states $\psi_+(x, y, 0) = u/\sqrt{|u|^2 + |v|^4}$ and $\psi_-(x, y, 0) = v/\sqrt{|u|^2 + |v|^4}$ are determined by the complex functions $u = 2(x + iy)f(r)/(1 + r^2)$ and $v = i[r^2 + 1 - f(r)]/(1 + r^2)$, respectively.

Our approach transforms the flow characterized by nonlinear vortex dynamics and a distinct body force into a linear two-component Schrödinger equation via the generalized Madelung transformation. Typically, converting nonlinear equations to linear form involves increasing the dimensionality^{26,61,62}, whereas the present approach, similar to the Cole-Hopf transformation⁶³, does not increase the dimensionality. Thus, we solve the linear Schrödinger equation, avoiding the challenge of nonlinearity. However, this merely serves as a demonstrative example of the flow simulation capabilities on NISQ devices. For a general form of the body force, or the Laplacian dissipation for Newtonian fluids in particular⁴⁸, the associated two-component Schrödinger equation becomes nonlinear. How to solve the nonlinear Schrödinger equations efficiently using quantum algorithms remains an open problem^{64–66}. In this flow with $V = 0$ in the Hamiltonian, the two components of the wave function decouple during the entire evolution, so that we can simulate their dynamics separately without using an additional qubit. The circuits for preparing ψ_+ and ψ_- , obtained based on CFlow, have depths of 23 and 27, respectively, which can prepare quantum states with overlaps above 0.993 to the target ones in the ideal case. We then evolve ψ_+ and ψ_- independently for specific times and measuring the corresponding densities ρ_{\pm} and momentum J_{\pm} , with the procedure similar to the diverging flow case. The velocity is then obtained by $\mathbf{u} = (\mathbf{J}_+ + \mathbf{J}_-)/(\rho_+ + \rho_-)$, which introduces the nonlinearity for vortex dynamics, and the vorticity is calculated as $\omega = \partial u_y/\partial x - \partial u_x/\partial y$.

Figure 3 (a),(b) plot the evolution of the ω -contour and streamlines from experimental and ideal results at $t = 0, \pi/4$, and $\pi/2$. Initial circular streamlines evolve into spirals with vorticity decay under the body force in the Schrödinger flow. The experimental results in Fig. 3(b) clearly capture the vortex evolution. The vorticity magnitude is underestimated due to quantum gate noises and sampling errors. At the vortex outer edge, the flow field exhibits turbulent artifacts which enhances vortex dissipation. It is accidental to observe that the energy spectrum of the noisy experimental data appears to exhibit the $k^{-5/3}$ scaling law as in classical turbulence (see Supplementary Fig. S10). Therefore, on the other hand, the NISQ hardware noises could potentially be leveraged to model small-scale turbulent motion⁶⁷.

The θ -averaged profiles for ω in Fig. 3c show the successful initial construction of the vortex using the two-component wave function. The

peak of $\langle \omega \rangle_{\theta}$ decays notably faster in the experimental results compared to the exact solution, due to the vortex being displaced from the domain center under spurious turbulent motion and the numerical error in computing ω with differentiation of noisy data.

Discussion

We have conducted experiments on the digital quantum simulation of unsteady fluid flows with a superconducting quantum processor. Our algorithm employs the hydrodynamic formulation of the Schrödinger equation, apt for unitary operations in quantum computing. The computational complexity for the state evolution (detailed in Supplementary Note 5) in Eq. (2) is $\mathcal{O}(n^2)$ ⁶⁸, with the total number of qubits $n = n_x + n_y$. This represents an exponential speedup over the classical counterpart whose complexity is $\mathcal{O}(n^{2n})$. The quantum simulations well capture the evolution of averaged profiles of the density and momentum in the 2D compressible diverging potential flow and the nonlinear decaying process of the 2D vortex. Our results showcase the capability of simulating fluid dynamics on NISQ devices, and indicate the promise of quantum computing in probing complex flow phenomena such as turbulence and transition in engineering applications.

Looking forward, despite the demonstration in the present work, realizing quantum advantage for the simulation of practical fluid flows with NISQ devices remains an outstanding challenge. The quantum representation employed in the present experiment with NISQ devices is tailored from the full quantum representation for the Navier-Stokes equation⁴⁷, with introducing the artificial body force into the flow. Therefore, methods such as increasing dimensionality^{69–71} should be explored to incorporate the nonlinearity and the non-Hermitian Hamiltonian of a general flow^{47,72} into the quantum algorithm. In addition, the preparation of initial quantum states for general velocity fields is an open problem^{46,73}. Variational quantum algorithms offer a promising approach to approximate the initial quantum state directly through numerical optimization⁷⁴. The full characterization of a flow field requires an exponentially large number of measurement shots, and it would be important to find flow statistics that can be measured efficiently without undermining the overall quantum advantage. Finally, the potential inclusion of quantum error correction is desired to fully harness the strengths of the quantum simulation of fluid dynamics.

Methods

Device and experimental setup

The quantum processor was fabricated using the flip-chip recipe, where all qubits and couplers are located on a top chip, and most of the control/readout lines and readout resonators are located on a bottom chip. These two chips have lithographically defined base wirings made of tantalum and junction loops made of aluminum, and are galvanically connected via indium bumps. The processor was loaded into a multilayer printed circuit board enclosure, which was then mounted inside a dilution refrigerator with the base temperature down to 15 mK. There are 11×11 frequency-tunable transmon qubits encapsulated in a square lattice on the quantum processor, and the adjacent qubits are connected by tunable couplers for realizing high-fidelity quantum gates which is essential for the experiment.

In this work, we select ten qubits to carry out the quantum simulation, as shown in Fig. 1c. We employ the native gate set $\{U(\theta, \varphi, \lambda), CZ\}$ to implement the desired experimental circuits, where $U(\theta, \varphi, \lambda) = R_z(\varphi)R_y(\theta)R_z(\lambda)$ denotes a generic single-qubit gate with three Euler angles, and CZ denotes the two-qubit CZ gate that fits the layout topology of our device. By optimizing the control procedure, we realize fidelities of 99.97% and 99.67% for parallel single- and two-qubit gates applied on the ten qubits used in this experiment, respectively.

Quantum representation of fluid flows

We encode the flow states in the n_{ψ} -component wave function $\psi \equiv [\psi_1, \dots, \psi_{n_{\psi}}]^T$, for potential flows with $n_{\psi} = 1$ and vortical flows with $n_{\psi} = 2$. With the generalized Madelung transform, the flow density,

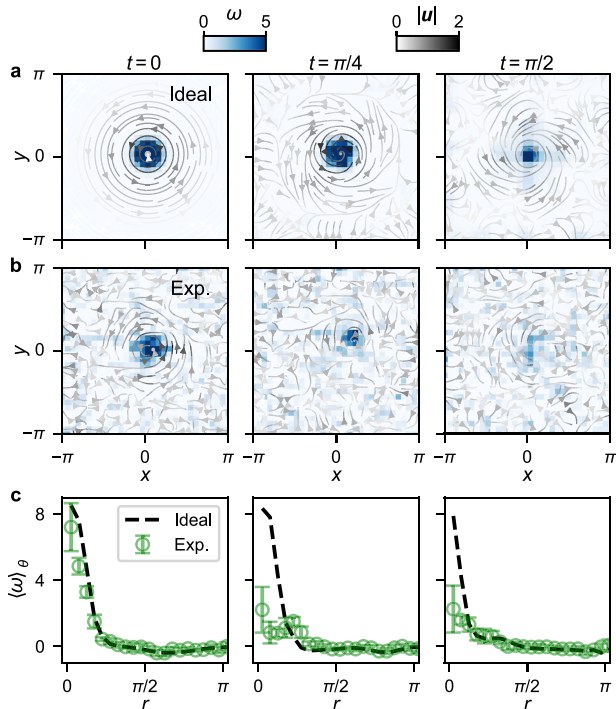


Fig. 3 | Comparison of experimental results on the superconducting quantum processor with the ideal ones for the 2D vortex. Vorticity contours are depicted for (a) the exact solution and (b) the experimental result. Streamlines are color-coded by velocity magnitude. c Comparison of $\langle \omega \rangle_\theta$ at $t = 0, \pi/4$, and $\pi/2$ (dashed lines: exact solution; circles: experimental result with error bars denoting one standard deviation), where $\langle \omega \rangle_\theta$ denotes the vorticity averaged over the θ -direction in polar coordinates (r, θ) . The data is obtained with 10^5 measurement shots, and the experiment is repeated for five times.

momentum, and velocity are $\rho \equiv \sum_{j=1}^{n_\psi} |\psi_j|^2$, $\mathbf{J} \equiv \frac{i\hbar}{2m} \sum_{j=1}^{n_\psi} (\psi_j \nabla \psi_j^* - \psi_j^* \nabla \psi_j)$, and $\mathbf{u} \equiv \mathbf{J}/\rho$, respectively.

Then, we consider a n_ψ -component time-dependent Schrödinger equation

$$i\hbar \frac{\partial}{\partial t} \psi_j = \left(-\frac{\hbar^2}{2m} \nabla^2 + V \right) \psi_j, \quad j \in \{1, \dots, n_\psi\} \quad (5)$$

with a real-valued potential V . The continuity equation

$$\frac{\partial \rho}{\partial t} + \nabla \cdot (\rho \mathbf{u}) = 0 \quad (6)$$

follows from the conservation of probability current. The momentum equation is obtained as a standard compressible Euler equation

$$\frac{\partial \mathbf{u}}{\partial t} + \mathbf{u} \cdot \nabla \mathbf{u} = -\frac{1}{\rho} \nabla p - \nabla U_F + \mathbf{f}, \quad (7)$$

with the pressure p , a conservative potential U_F , and a body force \mathbf{f} . For potential flows, we have $p = 0$, $U_F = V/m - \hbar^2 \nabla^2 \sqrt{\rho} / (2m^2 \sqrt{\rho})$, and $\mathbf{f} = \mathbf{0}$. For vortical flows, we have $p = \hbar \boldsymbol{\zeta} \cdot \mathbf{s} / m$, $U_F = V/m - \hbar^2 |\nabla \mathbf{s}|^2 / (8m^2 \rho^2)$, and $\mathbf{f} = \hbar \nabla \mathbf{s} \cdot \boldsymbol{\zeta} / (m\rho)$, with the spin vector $\mathbf{s} \equiv \boldsymbol{\psi}^* i \boldsymbol{\psi}$ and a vector $\boldsymbol{\zeta} \equiv -\nabla \cdot (\nabla \mathbf{s} / \rho) / 4$ (see Supplementary Note 1 for details).

Note that in practical fluid flows, the momentum equation does not include the term \mathbf{f} . This term can be regarded as an external body force with a dissipative effect^{45,75}. The corresponding ‘‘Schrödinger flow’’ can resemble the viscous flow in terms of the similar flow statistics and structures⁴⁵.

Circuit optimization

The preparation of an arbitrary n -qubit quantum state generally requires an order of 2^n quantum resources⁷⁶, either circuit depth or ancilla qubits, which is prohibitive for large n on the current device. Besides, the quantum circuits for realizing the QFT require further compilations to adapt the device topology. To circumvent these challenges, we adopt the CPFlow package recently introduced in ref. 59 to reduce the circuit depth for the initial state preparation and the state evolution.

The CPFlow is a variational circuit synthesis method. The program first use the parameterized controlled phase (CP) gates to integrate the discrete search into the continuous optimization procedure. The loss function is carefully designed to balance the fidelity among the optimized template, the target unitary (or state vector), and the circuit depth. After optimization, each CP gate is replaced by an identity (a CZ) gate if its angle lies within a threshold distance away from 0 (or π), or otherwise by their CZ decompositions. Once a prospective circuit is found, it is further optimized to obtained the final result. The fidelities of the optimized circuits and the corresponding depths for different simulation cases are listed in Supplementary Tables S1 and S2.

Detection of flow states

In our experiment, the flow density is obtained by measuring diagonal elements of the density matrix. The matrix elements of the measuring operator are

$$\hat{\rho}_{j,k}^{(m,l)} = \delta_{j,2^{n_x} m + l} \delta_{2^{n_x} m + l, k}, \quad (8)$$

where the indices $l = 0, 1, \dots, 2^{n_x} - 1$ and $m = 0, 1, \dots, 2^{n_y} - 1$ denote the discretized coordinates in the x - and y -directions, respectively.

For the momentum, we employ the finite difference method to approximate derivatives. The corresponding measuring operator (non-bounded) is expressed as

$$\hat{\mathbf{J}}_{j,k}^{(m,l)} = \frac{i}{2} \left[\delta_{2^{n_x} m + l, k} \left(\frac{\delta_{j,2^{n_x} m + l + 1} - \delta_{j,2^{n_x} m + l - 1}}{2\Delta x} \mathbf{e}_x + \frac{\delta_{j,2^{n_x} (m+1) + l} - \delta_{j,2^{n_x} (m-1) + l}}{2\Delta y} \mathbf{e}_y \right) - \delta_{j,2^{n_x} m + l} \left(\frac{\delta_{2^{n_x} m + l + 1, k} - \delta_{2^{n_x} m + l - 1, k}}{2\Delta x} \mathbf{e}_x + \frac{\delta_{2^{n_x} (m+1) + l, k} - \delta_{2^{n_x} (m-1) + l, k}}{2\Delta y} \mathbf{e}_y \right) \right]. \quad (9)$$

An intuitive strategy to obtain the momentum is quantum state tomography (QST). However, QST requires an exponentially increasing number of measurements, so it is impractical with a system size as large as ten qubits. Alternatively, we decompose each desired observable as a sum of Pauli strings and pick the necessary Pauli bases to infer expectation values of all required Pauli strings (see Supplementary Note 3 for details). As a result, the number of measurements is reduced to 62 in our work.

Consequently, the embedded flow state including the density and momentum can be extracted with 63 measurements. Each measurement involves 10^5 single shots to build the probability distribution, consuming approximately 20 s at a sampling rate of 5 kHz. The experiment is repeated five times for each flow case.

Data availability

The data presented in the figures and that support the other findings of this study are available for download at <https://doi.org/10.6084/m9.figshare.27173766> (ref. 77).

Code availability

The data analysis and numerical simulation codes for this study are available for download at <https://doi.org/10.6084/m9.figshare.27173766> (ref. 77).

Received: 22 June 2024; Accepted: 17 October 2024;

Published online: 25 October 2024

References

- Pope, S. B. *Turbulent Flows* (Cambridge University Press, 2000).
- Moin, P. & Mahesh, K. Direct numerical simulation: a tool in turbulence research. *Annu. Rev. Fluid Mech.* **30**, 539 (1998).
- Ishihara, T., Gotoh, T. & Kaneda, Y. Study of high-Reynolds number isotropic turbulence by direct numerical simulation. *Annu. Rev. Fluid Mech.* **41**, 165 (2009).
- Manin, Y. I. *Computable and Non-Computable*, Sovetskoe Radio, Moscow (1980).
- Benioff, P. The computer as a physical system: A microscopic quantum mechanical Hamiltonian model of computers as represented by Turing machines. *J. Stat. Phys.* **22**, 563 (1980).
- Feynman, R. P. Simulating physics with computers. *Int. J. Theor. Phys.* **21**, 467 (1982).
- Deutsch, D. Quantum theory, the Church-Turing principle and the universal quantum computer. *Proc. R. Soc. Lond. A* **400**, 97 (1985).
- Givi, P., Daley, A. J., Mavriplis, D. & Malik, M. Quantum speedup for aerospace and engineering. *AIAA J.* **58**, 8 (2020).
- Succi, S., Itani, W., Sreenivasan, K. & Steijl, R. Quantum computing for fluids: Where do we stand? *Europhys. Lett.* **144**, 10001 (2023).
- Bharadwaj, S. S. & Sreenivasan, K. R. Hybrid quantum algorithms for flow problems. *Proc. Natl Acad. Sci. USA.* **120**, e2311014120 (2023).
- Feynman, R., Leighton, R. and Sands, M. <https://books.google.com.sg/books?id=CL6DBQAAQBAJ> *The Feynman Lectures on Physics, Vol. II: The New Millennium Edition: Mainly Electromagnetism and Matter* (Basic Books, 2015).
- Daley, A. J. et al. Practical quantum advantage in quantum simulation. *Nature* **607**, 667 (2022).
- Kim, Y. et al. Evidence for the utility of quantum computing before fault tolerance. *Nature* **618**, 500 (2023).
- Hibat-Allah, M., Mauri, M., Carrasquilla, J. & Perdomo-Ortiz, A. A framework for demonstrating practical quantum advantage: comparing quantum against classical generative models. *Commun. Phys.* **7**, 68 (2024).
- Begušić, T., Gray, J. & Chan, G. K.-L. Fast and converged classical simulations of evidence for the utility of quantum computing before fault tolerance. *Sci. Adv.* **10**, eadk4321 (2024).
- Steijl, R. & Barakos, G. N. Parallel evaluation of quantum algorithms for computational fluid dynamics. *Comput. Fluids* **173**, 22 (2018).
- Gaitan, F. Finding flows of a Navier-Stokes fluid through quantum computing. *npj Quantum Inform.* **6**, 61 (2020).
- Chen, Z.-Y. et al. Quantum approach to accelerate finite volume method on steady computational fluid dynamics problems. *Quantum Inf. Process.* **21**, 137 (2022).
- Lapworth, L. A hybrid quantum-classical CFD methodology with benchmark HHL solutions. <https://arxiv.org/abs/2206.00419> (2022).
- Demirdjian, R., Gunlycke, D., Reynolds, C. A., Doyle, J. D. & Tafur, S. Variational quantum solutions to the advection-diffusion equation for applications in fluid dynamics. *Quantum Inf. Process.* **21**, 322 (2022).
- Gourianov, N. et al. A quantum-inspired approach to exploit turbulence structures. *Nat. Comput. Sci.* **2**, 30 (2022).
- Pfeffer, P., Heyder, F. & Schumacher, J. Hybrid quantum-classical reservoir computing of thermal convection flow. *Phys. Rev. Res.* **4**, 033176 (2022).
- Pfeffer, P., Heyder, F. & Schumacher, J. Reduced-order modeling of two-dimensional turbulent Rayleigh-Bénard flow by hybrid quantum-classical reservoir computing. *Phys. Rev. Res.* **5**, 043242 (2023).
- Jaksch, D., Givi, P., Daley, A. J. & Rung, T. Variational quantum algorithms for computational fluid dynamics. *AIAA J.* **61**, 1885 (2023).
- Liu, B., Zhu, L., Yang, Z. & He, G. Quantum implementation of numerical methods for convection-diffusion equations: toward computational fluid dynamics. *Commun. Comput. Phys.* **33**, 425 (2023).
- Succi, S., Itani, W., Sanavio, C., Sreenivasan, K. R. & Steijl, R. Ensemble fluid simulations on quantum computers. *Comput. Fluids* **270**, 106148 (2024).
- Au-Yeung, R., Williams, A. J., Kendon, V. M. & Lind, S. J. Quantum algorithm for smoothed particle hydrodynamics. *Comput. Phys. Commun.* **294**, 108909 (2024).
- Harrow, A. W., Hassidim, A. & Lloyd, S. Quantum algorithm for linear systems of equations. *Phys. Rev. Lett.* **103**, 150502 (2009).
- Costa, P. C. S. et al. Optimal scaling quantum linear-systems solver via discrete adiabatic theorem. *PRX Quantum* **3**, 040303 (2022).
- Aaronson, S. Read the fine print. *Nat. Phys.* **11**, 291 (2015).
- Preskill, J. Quantum computing in the NISQ era and beyond. *Quantum* **2**, 79 (2018).
- Bharti, K. et al. Noisy intermediate-scale quantum algorithms. *Rev. Mod. Phys.* **94**, 015004 (2022).
- Georgescu, I. M., Ashhab, S. & Nori, F. Quantum simulation. *Rev. Mod. Phys.* **86**, 153 (2014).
- Zhang, X. et al. Digital quantum simulation of Floquet symmetry-protected topological phases. *Nature* **607**, 468 (2022).
- Mi, X. et al. Time-crystalline eigenstate order on a quantum processor. *Nature* **601**, 531 (2022).
- Deng, J. et al. Observing the quantum topology of light. *Science* **378**, 966 (2022).
- Madelung, E. Quantentheorie in hydrodynamischer form. *Z. Phys.* **40**, 322 (1927).
- Yepez, J. Quantum lattice-gas model for computational fluid dynamics. *Phys. Rev. E* **63**, 046702 (2001).
- Mezzacapo, A. et al. Quantum simulator for transport phenomena in fluid flows. *Sci. Rep.* **5**, 13153 (2015).
- Joseph, I. Koopman-von Neumann approach to quantum simulation of nonlinear classical dynamics. *Phys. Rev. Res.* **2**, 043102 (2020).
- Budinski, L. Quantum algorithm for the advection-diffusion equation simulated with the lattice Boltzmann method. *Quantum Inf. Process.* **20**, 57 (2021).
- Itani, W. & Succi, S. Analysis of Carleman linearization of lattice Boltzmann. *Fluids* **7**, 24 (2022).
- Zylberman, J., Di Molfetta, G., Brachet, M., Loureiro, N. F. & Debbasch, F. Quantum simulations of hydrodynamics via the Madelung transformation. *Phys. Rev. A* **106**, 032408 (2022).
- Lu, Z. & Yang, Y. Quantum computing of reacting flows via Hamiltonian simulation. *Proc. Combust. Inst.* **40**, 105440 (2024).
- Meng, Z. & Yang, Y. Quantum computing of fluid dynamics using the hydrodynamic Schrödinger equation. *Phys. Rev. Res.* **5**, 033182 (2023).
- Meng, Z. & Yang, Y. Lagrangian dynamics and regularity of the spin Euler equation. *J. Fluid Mech.* **985**, A34 (2024).
- Meng, Z. & Yang, Y. Quantum spin representation for the Navier-Stokes equation. <https://arxiv.org/abs/2403.00596> (2024).
- Salasnich, L., Succi, S. & Tiribocchi, A. Quantum wave representation of dissipative fluids. *Int. J. Mod. Phys. C.* **35**, 2450100 (2024).
- Itani, W., Sreenivasan, K. R. & Succi, S. Quantum algorithm for lattice Boltzmann (QALB) simulation of incompressible fluids with a nonlinear collision term. *Phys. Fluids* **36**, 017112 (2024).
- Wright, L. et al. Noisy intermediate-scale quantum simulation of the one-dimensional wave equation. <https://arxiv.org/abs/2402.19247> (2024).
- Sanavio, C., Scatamacchia, R., de Falco, C. & Succi, S. Three Carleman routes to the quantum simulation of classical fluids. *Phys. Fluids* **36**, 057143 (2024).

52. Sanavio, C. & Succi, S. Lattice Boltzmann-Carleman quantum algorithm and circuit for fluid flows at moderate Reynolds number. *AVS Quantum Sci.* **6**, 023802 (2024).
53. Xu, S. et al. Digital Simulation of Projective Non-Abelian Anyons with 68 Superconducting Qubits. *Chin. Phys. Lett.* **40**, 060301 (2023).
54. Xu, S. et al. Non-Abelian braiding of Fibonacci anyons with a superconducting processor. *Nat. Phys.* **20**, 1469 (2024).
55. Bao, Z. et al. Creating and controlling global Greenberger-Horne-Zeilinger entanglement on quantum processors. *Nat. Commun.* **15**, 8823 (2024).
56. Trotter, H. On the Product of Semi-Groups of Operators. *Proc. Am. Math. Soc.* **10**, 545 (1959).
57. Kelly, J. et al. Optimal Quantum Control Using Randomized Benchmarking. *Phys. Rev. Lett.* **112**, 240504 (2014).
58. Ren, W. et al. Experimental Quantum Adversarial Learning with Programmable Superconducting Qubits. *Nat. Comput. Sci.* **2**, 711 (2022).
59. Nemkov, N. A., Kiktenko, E. O., Luchnikov, I. A. & Fedorov, A. K. Efficient variational synthesis of quantum circuits with coherent multi-start optimization. *Quantum* **7**, 993 (2023).
60. Kedia, H., Foster, D., Dennis, M. R. & Irvine, W. T. M. Weaving knotted vector fields with tunable helicity. *Phys. Rev. Lett.* **117**, 274501 (2016).
61. Liu, J.-P. et al. Efficient quantum algorithm for dissipative nonlinear differential equations. *Proc. Natl Acad. Sci. Usa.* **118**, e2026805118 (2021).
62. Tennie, F. & Magri, L. Solving nonlinear differential equations on quantum computers: A Fokker-Planck approach. <https://arxiv.org/abs/arXiv:2401.13500> (2024).
63. Evans, L. C. *Partial Differential Equations*, Vol. 19 (American Mathematical Society, 2022).
64. Lubasch, M., Joo, J., Moinier, P., Kiffner, M. & Jaksch, D. Variational quantum algorithms for nonlinear problems. *Phys. Rev. A* **101**, 010301(R) (2020).
65. Großardt, A. Nonlinear-ancilla aided quantum algorithm for nonlinear Schrödinger equations. <https://arxiv.org/abs/arXiv:2403.10102> (2024).
66. Tennie, F., Laizet, S., Lloyd, S. & Magri, L. Quantum computing for nonlinear differential equations and turbulence. <https://arxiv.org/abs/arXiv:2406.04826> (2024).
67. Pope, S. B. Simple models of turbulent flows. *Phys. Fluids* **23**, 011301 (2011).
68. Nielsen, M. A. & Chuang, I. L. *Quantum Computation and Quantum Information*, 10th ed. (Cambridge University Press, New York, 2010).
69. Lloyd, S. et al. Quantum algorithm for nonlinear differential equations. <https://arxiv.org/abs/arXiv:2011.06571> (2020).
70. Jin, S., Liu, N. & Yu, Y. Quantum simulation of partial differential equations: Applications and detailed analysis. *Phys. Rev. A* **108**, 032603 (2023).
71. Koukoutsis, E., Hizanidis, K., Ram, A. K. & Vahala, G. Dyson maps and unitary evolution for Maxwell equations in tensor dielectric media. *Phys. Rev. A* **107**, 042215 (2023).
72. Ashida, Y., Gong, Z. & Ueda, M. Non-Hermitian physics. *Adv. Phys.* **69**, 249 (2021).
73. Yang, Y., Xiong, S. & Lu, Z. Applications of the vortex-surface field to flow visualization, modelling and simulation. *Flow* **3**, E33 (2023).
74. Su, H., Xiong, S. & Yang, Y. Quantum state preparation for a velocity field based on the spherical Clebsch wave function. <https://arxiv.org/abs/arXiv:2406.04652> (2024).
75. Chern, A., Knöppel, F., Pinkall, U., Schröder, P. & Weißmann, S. Schrödinger's smoke. *ACM Trans. Graph.* **35**, 1 (2016).
76. Gui, K., Dalzell, A. M., Achille, A., Suchara, M. & Chong, F. T. Spacetime-Efficient Low-Depth Quantum State Preparation with Applications. *Quantum* **8**, 1257 (2024).
77. Xu, S. <https://doi.org/10.6084/m9.figshare.27173766> Simulating unsteady flows on a superconducting quantum processor Figshare (2024).

Acknowledgements

The device was fabricated at the Micro-Nano Fabrication Center of Zhejiang University. This work has been supported by the National Key R&D Program of China (Grant No. 2023YFB4502600), the National Natural Science Foundation of China (Grant Nos. 11925201, 11988102, 12174342, 12274367, 12274368, 12322414, and 92365301), the Zhejiang Provincial Natural Science Foundation of China (Grant Nos. LR24A040002 and LDQ23A040001), and the New Cornerstone Science Foundation through the XPLOERER Prize.

Author contributions

Y.Y. conceived the theoretical ideas. J.Z. and S.X. carried out the experiment under the supervision of C.S. J.C. and X.Z. designed the device and H.L. fabricated the device, supervised by H.W. Z.M. designed the digital quantum circuits under the supervision of Y.Y. Z.M., J.Z., S.X., K.W., S.-Y.X., and Y.Y. conducted the theoretical analysis. J.Z., S.X., K.W., J.C., F.J., X.Z., Y.G., Y.W., C.Z., N.W., Y.Z., A.Z., Z.C., F.S., Z.B., Z.Z., P.Z., Z.T., T.L., H.L., Q.G., Z.W., C.S. and H.W. contributed to the experimental setup. All authors contributed to the analysis of data, discussion of the results, and writing of the manuscript.

Competing interests

The authors declare no competing interests.

Additional information

Supplementary information The online version contains supplementary material available at <https://doi.org/10.1038/s42005-024-01845-w>.

Correspondence and requests for materials should be addressed to Chao Song or Yue Yang.

Peer review information *Communications Physics* thanks Sauro Succi and the other, anonymous, reviewers for their contribution to the peer review of this work. A peer review file is available.

Reprints and permissions information is available at <http://www.nature.com/reprints>

Publisher's note Springer Nature remains neutral with regard to jurisdictional claims in published maps and institutional affiliations.

Open Access This article is licensed under a Creative Commons Attribution-NonCommercial-NoDerivatives 4.0 International License, which permits any non-commercial use, sharing, distribution and reproduction in any medium or format, as long as you give appropriate credit to the original author(s) and the source, provide a link to the Creative Commons licence, and indicate if you modified the licensed material. You do not have permission under this licence to share adapted material derived from this article or parts of it. The images or other third party material in this article are included in the article's Creative Commons licence, unless indicated otherwise in a credit line to the material. If material is not included in the article's Creative Commons licence and your intended use is not permitted by statutory regulation or exceeds the permitted use, you will need to obtain permission directly from the copyright holder. To view a copy of this licence, visit <http://creativecommons.org/licenses/by-nc-nd/4.0/>.

© The Author(s) 2024